Image reconstruction in optical tomography in the presence of coupling errors

Martin Schweiger, Ilkka Nissilä, David A. Boas, and Simon R. Arridge

Image reconstruction in optical tomography is a nonlinear and generally ill-posed inverse problem. Noise in the measured surface data can give rise to substantial artifacts in the recovered volume images of optical coefficients. Apart from random shot noise caused by the limited number of photons detected at the measurement site, another class of systematic noise is associated with losses specific to individual source and detector locations. A common cause for such losses in data acquisition systems based on fiber-optic light delivery is the imperfect coupling between the fiber tips and the skin of the patient because of air gaps or surface moisture. Thus the term coupling errors was coined for this type of data noise. However, source and detector specific errors can also occur in noncontact measurement systems not using fiber-optic delivery, for example, owing to local skin pigmentation, hair and hair follicles, or instrumentation calibration errors. Often it is not possible to quantify coupling effects in a way that allows us to remove them from the data or incorporate them into the light transport model. We present an alternative method of eliminating coupling errors by regarding the complex-valued coupling factors for each source and detector as unknowns in the reconstruction process and recovering them simultaneously with the images of absorption and scattering. Our method takes into account the possibility that coupling effects have an influence on both the amplitude and the phase shift of the measurements. Reconstructions from simulated and experimental phantom data are presented, which show that including the coupling coefficients in the reconstruction greatly improves the recovery of absorption and scattering images.

OCIS codes: 100.3190, 170.3010, 110.4280.

1. Introduction

Diffuse optical tomography is a novel medical imaging modality[1–3] that seeks to reconstruct 3D images of tissue optical parameters and related functional images of tissue physiology, such as blood volume and oxygenation,[4] particularly in peripheral muscle, breast tissue,[5] and the brain.[6–9] Data acquisition systems deliver light to the surface of the body and measure the light transmitted through the tissue at multiple detector locations on the surface. Due to high scattering of IR light by biological tissue, the relationship between volume parameters and measurements is nonlinear, and the measurement data carry little spatial information, which generally requires an iterative and regularized model-based approach to image reconstruction. We have previously presented a reconstruction algorithm that uses a finite element model for simulating diffuse light propagation in scattering media and a regularized Newton–Krylov approach to image reconstruction of the absorption and scattering distribution inside a 3D volume from boundary measurements of modulation amplitude and phase shift of radio-frequency-modulated input sources.[10] This model assumes constant coupling between each fiber and the tissue or phantom and perfect calibration of the instrument, without losses in the light delivery setup or at the skin surface. In practice such losses do occur and must be included in the model to avoid the propagation of noise into the image. In this paper we will extend the current image reconstruction scheme to account for a class of systematic noise known as coupling errors. By this we understand errors in amplitude and phase that are specific to individual source and detector channels but do not vary tempo-

M. Schweiger (M.Schweiger@cs.ucl.ac.uk) and S. R. Arridge are with the Centre for Medical Image Computing, University College London, London WC1E 6BT, UK. I. Nissilä is with D. A. Boas at the Athinoula A. Martinos Center for Biomedical Imaging, Massachusetts General Hospital, 149 13th Street, Charlestown, Massachusetts 02129, USA, and is also at the Laboratory of Biomedical Engineering, Helsinki University of Technology, P.O. Box 2200, 02015 HUT, Helsinki, Finland.

Received 4 August 2006; revised 21 December 2006; accepted 6 January 2007; posted 10 January 2007 (Doc. ID 73784); published 23 April 2007.

0003-6935/07/142743-14$15.00/0

rally. The most common cause for this type of error is the imperfect delivery or collection of light on the surface owing to losses at the interface between the skin and light delivery system. In many data acquisition systems, light is delivered and collected by optical fibers. In these systems, it is possible that an air gap between the fiber tip and the skin surface affects the characteristics of light delivery. Hair and local skin surface features, such as moles and follicles, will also have an influence on the coupling where surface areas of light delivery and collection are small, as is commonly the case for fiber-based systems. Other channel-specific effects, such as losses in individual optical fibers or differences in detector gain, can also be included in the coupling parameters.

Since coupling effects are difficult to predict and quantify, they cannot normally be included directly in the light transport model. Instead we propose to treat them as unknowns and include them in the reconstruction process. A previous study by Boas *et al.*[11] has used a similar approach for amplitude calibration only, and promising results of absorption reconstruction from simulated data were presented. Stott *et al.*[12] have extended this method to include the correction for positional errors in the source and detector locations. Schmitz *et al.*[13] have presented a method of calculating real-valued source and detector coupling coefficients for a linear transfer function used for measuring dynamic changes with a CCD detection system.

Oh *et al.*[14] have expressed the problem of coupling coefficient recovery in a Bayesian regularization framework, where optical parameters and coupling coefficients were updated sequentially in each iteration step of the nonlinear maximum *a posteriori* reconstruction scheme. Other authors[15–17] showed that errors induced by the measurement system can be reduced by incorporating reference measurements obtained from phantoms with known optical properties. Recent work on calibrating measurement data to account for coupling effects includes Tarvainen *et al.*[18] and Nissilä *et al.*[19]

In this paper we present a method that takes into account coupling factors for both the amplitude and phase data obtained from frequency domain data acquisition systems. Phase coupling can occur, for example, from reflections in the optical system or dispersion of the signal in the fiber. We will show that the reconstruction algorithm can recover amplitude and phase coupling coefficients in addition to the simultaneous reconstruction of absorption and scattering images and that the inclusion of the coupling coefficients can improve convergence and image quality dramatically. The results from applying the method to both simulated and experimental data will be presented.

2. Forward Problem with Coupling Coefficients

A. Light Transport Model

Consider the problem of light propagation in a highly scattering domain Ω bounded by $\partial\Omega$, where absorption coefficient $\mu_a(\mathbf{r})$ and scattering coefficient $\mu_s(\mathbf{r})$ satisfy $\mu_s(\mathbf{r}) \gg \mu_a(\mathbf{r})$ everywhere. Further let the distance between the boundary source and detector locations be large compared to the mean free transport path $1/\mu_s$. Then the diffusion equation[20,21] is an adequate model for light transport in Ω.[22,23] In the frequency domain, the diffusion equation is given by

$$\left(-\nabla \cdot \kappa(\mathbf{r})\nabla + \mu_a(\mathbf{r}) + \frac{i\omega}{c}\right)\phi(\mathbf{r},\ \omega) = q(\mathbf{r},\ \omega), \quad \mathbf{r} \in \Omega, \tag{1}$$

where κ is the diffusion coefficient given by $\kappa = 1/[3(\mu_a + \mu_s')]$, with $\mu_s' = (1 - g)\mu_s$ and g being the anisotropy coefficient for the single-scattering phase function. q is the boundary source distribution modulated at frequency ω, and ϕ is the photon density field in the medium. Where the diffusion equation is not sufficient, a higher-order approximation to the Boltzmann equation must be used.[24,25] The discussion of coupling coefficients in this paper can be applied directly to these models. We employ a Robin boundary condition:

$$\phi(\xi,\ \omega) + 2\kappa(\xi)\zeta\nabla_n\phi(\xi,\ \omega) = 0, \quad \xi \in \partial\Omega, \tag{2}$$

where ζ is a coefficient that incorporates the refractive index mismatch at the tissue–air interface, and operator ∇_n denotes the outward normal to the boundary at point ξ. The complex boundary flux Γ is obtained by boundary operator

$$\Gamma(\xi) = -\kappa(\xi)\nabla_n\phi(\xi,\ \omega) = \frac{1}{2\zeta}\,\phi(\xi,\ \omega), \quad \xi \in \partial\Omega. \tag{3}$$

Consider a data acquisition system consisting of S boundary source distributions $q_i(\xi)$, $\xi \in \partial\Omega$, $i = 1 \ldots S$, which are illuminated sequentially, and M boundary detectors, with sensitivity profiles $w_j(\xi)$, $j = 1 \ldots M$, along the boundary. Then the signal $y_{ij} \in \mathbb{C}$ measured by detector j under illumination from source i is given by

$$y_{ij} = \int_{\partial\Omega} w_j(\xi)\Gamma_i(\xi)\mathrm{d}\xi = \int_{\partial\Omega} \frac{w_j(\xi)}{2\zeta}\,\phi_i(\xi,\ \omega)\mathrm{d}\xi, \tag{4}$$

where ϕ_i is the solution to Eq. (1) for source distribution q_i. The forward problem [Eqs. (1)–(4)] may be formally represented by the operator

$$\mathbf{y} = f(\mathbf{x}), \tag{5}$$

where $\mathbf{y} \in \mathbb{C}^{SM}$ is the vector of complex projection data, and $\mathbf{x} = \{\mu_i, \kappa_i\} \in \mathbb{R}^{2B}$ is an array of basis coefficients for the optical parameters κ and μ, expressed in a suitable spatial basis expansion $b_k(\mathbf{r})$ of dimension B, such that a parameter distribution $x(\mathbf{r})$ can be approximated by

$$x(\mathbf{r}) \approx \sum_{k=1}^{B} x_k b_k(\mathbf{r}), \tag{6}$$

where $\{x_k\}$ is a $2B$-dimensional vector of basis coefficients. We have implemented the model Eq. (5) as a finite-element model (FEM), by subdividing domain Ω into nonoverlapping elements of simple shape, such as tetrahedra or regular voxels, and defining a basis consisting of local polynomial basis functions.[26,27]

B. Coupling Coefficients

We now consider each source q_i to be contaminated linearly with a coupling coefficient $\alpha_i \in \mathbb{C}$, producing a modified field

$$\tilde{\phi}_i(\mathbf{r}, \omega) = \alpha_i \phi_i(\mathbf{r}, \omega), \quad i = 1 \ldots S, \tag{7}$$

and each measurement to be contaminated with a coupling coefficient $\beta_j \in \mathbb{C}$, producing modified data

$$\tilde{\Gamma}_{ij}(\xi) = \beta_j \frac{1}{2\zeta} \tilde{\phi}_i(\xi, \omega) = \alpha_i \beta_j \Gamma_{ij}(\xi), \quad i = 1 \ldots S,$$
$$j = 1 \ldots M, \tag{8}$$

leading to a modified forward operator

$$\tilde{\mathbf{y}} = \tilde{f}(\tilde{\mathbf{x}}), \tag{9}$$

where the augmented solution vector $\tilde{\mathbf{x}}$ now includes the unknown coupling coefficients, $\tilde{\mathbf{x}} = \{\mathbf{x}, \alpha, \beta\}$, and the forward model is modified by the multiplicative coefficients

$$\tilde{f}_{ij}(\tilde{\mathbf{x}}) = \alpha_i \beta_j f_{ij}(\mathbf{x}). \tag{10}$$

Note that as each measurement is affected by a product $\alpha_i \beta_j$ of two coupling coefficients, the set of coefficients $\{\alpha, \beta\}$ is uniquely defined only up to an arbitrary scaling factor[11] $\eta \in \mathbb{C}$: $\{\eta\alpha, \eta^{-1}\beta\}$. In the iterative reconstruction algorithm described below this ambiguity is implicitly taken into account by recovering coupling coefficients that minimally vary from their initial estimates $\{\alpha^{(0)}, \beta^{(0)}\}$, such that

$$\eta = \arg\min_{\bar{\eta}} \Big[\sum_i (\bar{\eta}\alpha_i - \alpha_i^{(0)})^2 + \sum_j (\bar{\eta}^{-1}\beta_j - \beta_j^{(0)})^2 \Big]. \tag{11}$$

3. Inverse Solver

We have previously presented a damped Gauss–Newton scheme for recovering the optical parameters from boundary measurements,[10] which uses a Krylov solver with implicit representation of the Hessian matrix to solve the linearized problem at each Gauss–Newton step k:

$$\mathbf{x}_{k+1} = \mathbf{x}_k + \gamma_k \big[\mathbf{J}^T(\mathbf{x}_k)\mathbf{J}(\mathbf{x}_k) + \tau\psi''(\mathbf{x}_k) \big]^{-1} \big[\mathbf{J}^T(\mathbf{x}_k)(\mathbf{y} - f(\mathbf{x}_k)) - \tau\psi'(\mathbf{x}_k) \big] \tag{12}$$

where $\mathbf{J}$ is the Jacobian of the forward model, ψ is a regularization term with ψ' and ψ'' being its first and second derivatives with respect to the parameters $\mathbf{x}_k$, and τ is a regularization hyperparameter. γ_k is a step length obtained by a line search at each iteration.

To extend this solver to the simultaneous reconstruction of the optical and coupling coefficients, $\mathbf{x}$ must be replaced by the augmented solution vector $\tilde{\mathbf{x}}$, forward model f by the extended model $\tilde{f}$ defined in Eq. (10), and the Jacobian $\mathbf{J}$ by an augmented matrix $\tilde{\mathbf{J}}$ that includes the derivatives of the projection data with respect to the source and detector coupling coefficients.

A. Calculation of the Jacobian

The nonlinear reconstruction scheme for recovery of the optical parameters $\mathbf{x}$ now must be adapted to recover the extended solution vector $\tilde{\mathbf{x}}$ including the

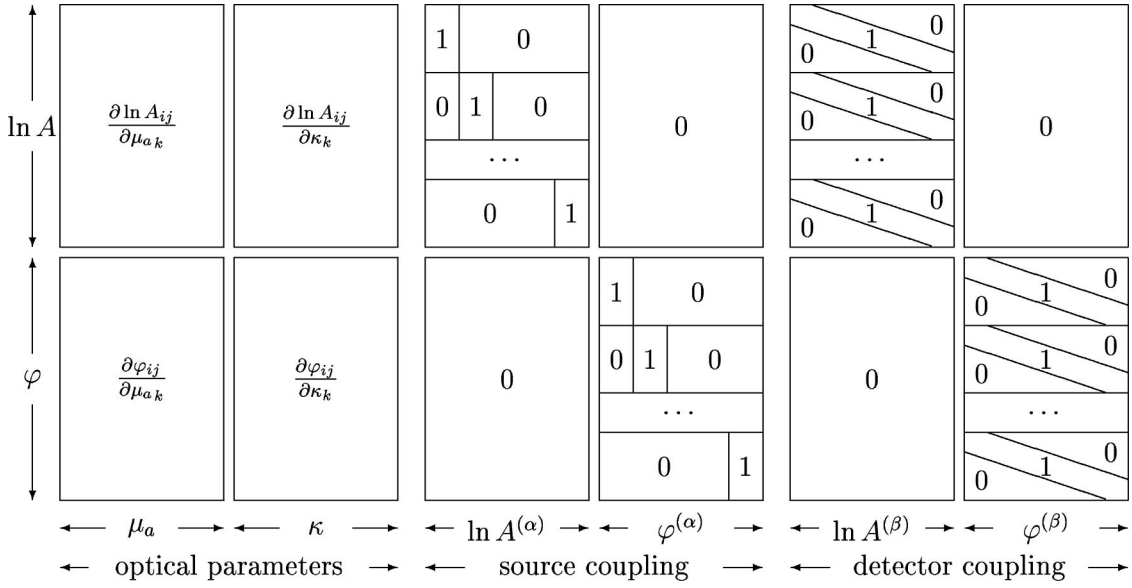

Fig. 1. Block structure of the augmented Jacobian including optical parameters, source and detector coupling blocks.

coupling coefficients. Our reconstruction approach uses a Gauss–Newton scheme that requires the calculation of the Jacobian of the forward model, $\mathbf{J}_{ij,k} = \partial f_{ij}(\mathbf{x})/\partial x_k$. After extending for the additional coupling coefficient parameters in the solution vector, this becomes

$$\tilde{\mathbf{J}} = \left[\frac{\partial \tilde{f}_{ij}(\tilde{\mathbf{x}})}{\partial x_k} \quad \frac{\partial \tilde{f}_{ij}(\tilde{\mathbf{x}})}{\partial \alpha_l} \quad \frac{\partial \tilde{f}_{ij}(\tilde{\mathbf{x}})}{\partial \beta_m} \right]. \tag{13}$$

With Eq. (10), the components of the modified Jacobian are evaluated as

$$\frac{\partial \tilde{f}_{ij}(\tilde{\mathbf{x}})}{\partial x_k} = \alpha_i \beta_j \frac{\partial f_{ij}(\mathbf{x})}{\partial x_k}, \tag{14}$$

$$\frac{\partial \tilde{f}_{ij}(\tilde{\mathbf{x}})}{\partial \alpha_l} = \begin{cases} \beta_j f_{ij}(\mathbf{x}) & \text{if } i = l \\ 0 & \text{otherwise,} \end{cases} \tag{15}$$

$$\frac{\partial \tilde{f}_{ij}(\tilde{\mathbf{x}})}{\partial \beta_m} = \begin{cases} \alpha_i f_{ij}(\mathbf{x}) & \text{if } j = m \\ 0 & \text{otherwise.} \end{cases} \tag{16}$$

Commonly the measurements are expressed in logarithmic polar form, in terms of logarithmic amplitude and phase:

$$y_{ij} = A_{ij} \exp \mathrm{i}\varphi_{ij} \Rightarrow \begin{cases} \ln A_{ij} = \mathrm{Re}(\ln y_{ij}) \\ \varphi_{ij} = \mathrm{Im}(\ln y_{ij}) \end{cases}. \tag{17}$$

Similarly, the coupling coefficients can be expressed in polar form:

$$\alpha_i = A_i^{(\alpha)} \exp \mathrm{i}\varphi_i^{(\alpha)}, \qquad \beta_j = A_j^{(\beta)} \exp \mathrm{i}\varphi_i^{(\beta)}. \tag{18}$$

Recasting Eq. (10) in logarithmic form leads to

$$\hat{f}_{ij}(\tilde{\mathbf{x}}) := \ln \tilde{f}_{ij}(\tilde{\mathbf{x}}) = \ln(\tilde{A}_{ij}) + \mathrm{i}(\tilde{\varphi}_{ij}), \tag{19}$$

with

$$\tilde{A}_{ij} = A_{ij} A_i^{(\alpha)} A_j^{(\beta)}, \qquad \tilde{\varphi}_{ij} = \varphi_{ij} + \varphi_i^{(\alpha)} + \varphi_j^{(\beta)}. \tag{20}$$

The Jacobian $\hat{\mathbf{J}}$ for $\hat{f}$ is organized so that the amplitude and phase components are stored in separate blocks, leading to a real-valued matrix:

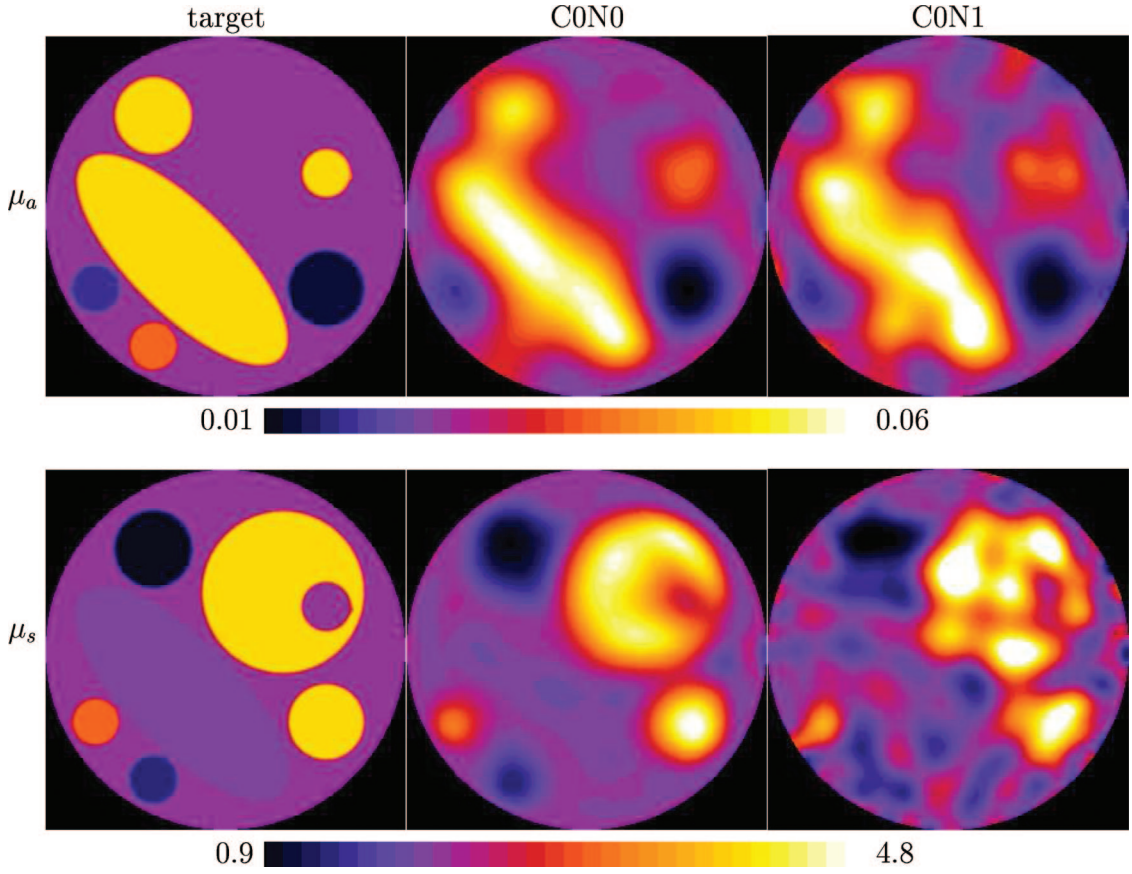

Fig. 2. (Color online) Target and reconstructed images of absorption (top) and scattering distributions (bottom) for the 2D test case. Image columns from left to right: target, reconstruction from noise-free data, and reconstruction from data with 1% additive Gaussian noise.

$$\hat{\mathbf{J}} = \begin{bmatrix} \frac{\partial \ln \tilde{A}_{ij}}{\partial \mu_{a\,k}} & \frac{\partial \ln \tilde{A}_{ij}}{\partial \kappa_k} & \frac{\partial \ln \tilde{A}_{ij}}{\partial \ln A_k^{(\alpha)}} & \frac{\partial \ln \tilde{A}_{ij}}{\partial \varphi_k^{(\alpha)}} & \frac{\partial \ln \tilde{A}_{ij}}{\partial \ln A_k^{(\beta)}} & \frac{\partial \ln \tilde{A}_{ij}}{\partial \varphi_k^{(\beta)}} \\ \frac{\partial \tilde{\varphi}_{ij}}{\partial \mu_{a\,k}} & \frac{\partial \tilde{\varphi}_{ij}}{\partial \kappa_k} & \frac{\partial \tilde{\varphi}_{ij}}{\partial \ln A_k^{(\alpha)}} & \frac{\partial \tilde{\varphi}_{ij}}{\partial \varphi_k^{(\alpha)}} & \frac{\partial \tilde{\varphi}_{ij}}{\partial \ln A_k^{(\beta)}} & \frac{\partial \tilde{\varphi}_{ij}}{\partial \varphi_k^{(\beta)}} \end{bmatrix}, \tag{21}$$

where the individual blocks are given by

$$\frac{\partial \ln \tilde{A}_{ij}}{\partial x_k} = \frac{1}{A_{ij}} \frac{\partial A_{ij}}{\partial x_k} = \frac{\partial \ln A_{ij}}{\partial x_k}, \tag{22}$$

$$\frac{\partial \tilde{\varphi}_{ij}}{\partial x_k} = \frac{\partial \varphi_{ij}}{\partial x_k}, \tag{23}$$

$$\frac{\partial \ln \tilde{A}_{ij}}{\partial \ln A_k^{(\alpha)}} = \begin{cases} 1 & \text{if } i = k \\ 0 & \text{otherwise} \end{cases}, \tag{24}$$

$$\frac{\partial \tilde{\varphi}_{ij}}{\partial \ln A_k^{(\alpha)}} = 0, \tag{25}$$

$$\frac{\partial \ln \tilde{A}_{ij}}{\partial \ln A_k^{(\beta)}} = \begin{cases} 1 & \text{if } j = k \\ 0 & \text{otherwise} \end{cases}, \tag{26}$$

$$\frac{\partial \tilde{\varphi}_{ij}}{\partial \ln A_k^{(\beta)}} = 0, \tag{27}$$

$$\frac{\partial \ln \tilde{A}_{ij}}{\partial \varphi_k^{(\alpha)}} = 0, \tag{28}$$

$$\frac{\partial \tilde{\varphi}_{ij}}{\partial \varphi_k^{(\alpha)}} = \begin{cases} 1 & \text{if } i = k \\ 0 & \text{otherwise} \end{cases}, \tag{29}$$

$$\frac{\partial \ln \tilde{A}_{ij}}{\partial \varphi_k^{(\beta)}} = 0, \tag{30}$$

$$\frac{\partial \tilde{\varphi}_{ij}}{\partial \varphi_k^{(\beta)}} = \begin{cases} 1 & \text{if } j = k \\ 0 & \text{otherwise} \end{cases}. \tag{31}$$

Table 1. Levels of Coupling and Random Error in the Simulated Data Sets Used for 2D Reconstructions

	Coupling Error		Relative Random Error
Data Set	$\sigma(\ln A^{(\alpha,\beta)})$	$\sigma(\varphi^{(\alpha,\beta)})$	$\sigma_R(\ln A, \varphi)$
C0N0	0	0	0
C1N0	0.2	0.01	0
C2N0	1	0.05	0
C3N0	2	0.1	0
C0N1	0	0	0.01
C1N1	0.2	0.01	0.01
C2N1	1	0.05	0.01
C3N1	2	0.1	0.01

The block structure of the resulting matrix is shown in Fig. 1. Whereas the blocks relating to the optical coefficients are dense, the coupling coefficient components are sparse.

B. Parameter Scaling

Due to the heterogeneity of both the data and parameter spaces, a rescaling of both spaces is necessary to compensate for ill conditioning of the linearized problem.[10] For the augmented solution vector $\tilde{\mathbf{x}}$, scaling of the parameter space now must also incorporate the coupling coefficients.

In this paper we use the solution space transformation

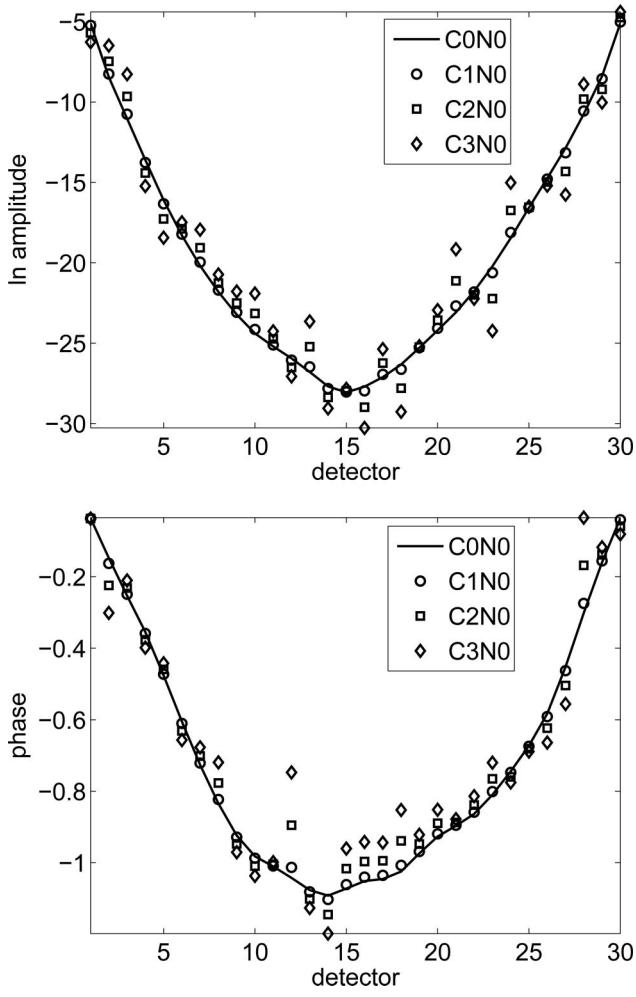

Fig. 3. Log amplitude and phase data at all detectors for a single source. Data without coupling contamination (solid curve) and with the three cases of coupling coefficients.

$$\tilde{\mathbf{x}} \rightarrow \mathrm{T}(\tilde{\mathbf{x}}) = \left\{ \ln \frac{\mu_a}{\bar{\mu}_a^{(0)}}, \ln \frac{\kappa}{\bar{\kappa}^{(0)}}, \ln \frac{\alpha}{\bar{\alpha}^{(0)}}, \ln \frac{\beta}{\bar{\beta}^{(0)}} \right\}, \tag{32}$$

where each of the components is rescaled by the average of its initial estimate, indicated by superscript 0, and then transformed to its logarithm.

The Jacobian **J** has to be rescaled accordingly. The data and solution space transformations are represented by the premultiplication and postmultiplication with a diagonal matrix, respectively. For more details on the application of data and solution space transformations see Ref. 10.

4. Results

A. Simulated Two-Dimensional Data

To assess the effectiveness of the coupling coefficient recovery, reconstructions from simulated 2D data contaminated with artificial coupling coefficients were performed. The target image is a circle of radius 25 mm with embedded circular and elliptical absorption and scattering objects (Fig. 2). The background parameters are $\mu_a = 0.025\ \mathrm{mm}^{-1}$ and $\mu_s = 2\ \mathrm{mm}^{-1}$. The parameter ranges of the inclusions are $0.01\ \mathrm{mm}^{-1} < \mu_a < 0.06\ \mathrm{mm}^{-1}$ and $0.8\ \mathrm{mm}^{-1} < \mu_s < 5\ \mathrm{mm}^{-1}$.

Data are generated for 32 source and 32 detector positions evenly spaced along the circumference of the object. Each measurement consists of logarithmic amplitude $\ln A$ and phase φ at a modulation frequency of 100 MHz, using a finite-element mesh discretization consisting of 32,971 nodes and 7261 ten-noded triangles, supporting a piecewise cubic polynomial basis expansion.

The forward model employed by the reconstruction algorithm uses a lower-resolution mesh with 1015 nodes, 1950 three-noded triangles, and a piecewise linear basis expansion. The FEM data are mapped into a regular bilinear basis grid with dimensions of 40×40. After removing the grid points outside the support of the domain, the basis is represented by 1332 basis coefficients. The dimensions of the real-valued solution space is thus $1332 \times 2 + (32 + 32) \times 2 = 2772$, including 2664 optical coefficients and 128 coupling coefficients.

For reference, Fig. 2 shows the result of a reconstruction of the optical parameters only from data that are not contaminated by coupling coefficients,

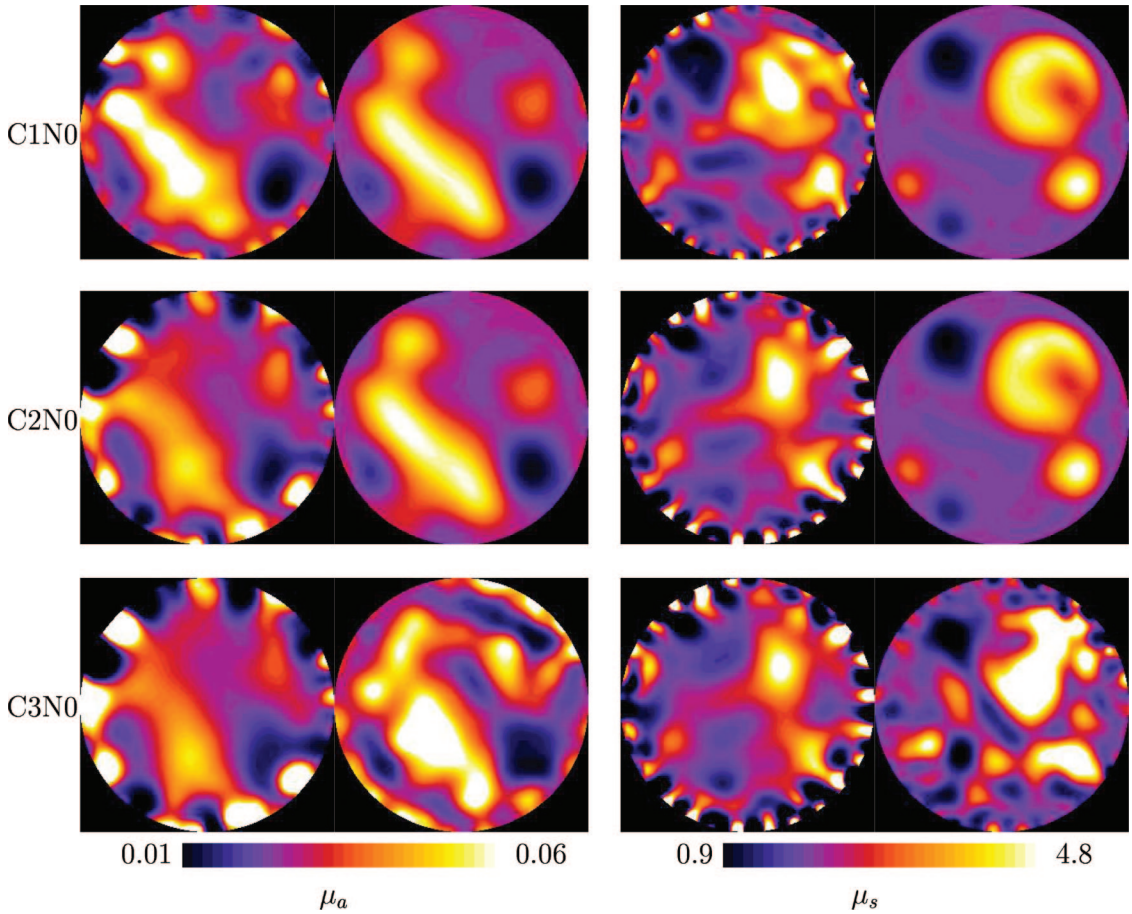

Fig. 4. (Color online) Reconstructions from data in the presence of coupling errors. Shown are absorption images (left) and scattering images (right) for the three levels of coupling contamination, without additional random noise. In each image pair, the left image shows the conventional reconstruction without accounting for coupling noise, while the right image is obtained when coupling coefficients are included in the reconstruction.

both without additional random data noise and with added Gaussian noise at a level of $\sigma = 1\%$. These results have been presented previously and show good localization and quantitative recovery of the inclusions for the noiseless case, and some degradation of the recovered shape of the inclusions when data noise is present.

The simulated projection data are then contaminated by adding synthetic source coupling coefficients $\ln A^{(\alpha)}$, $\varphi^{(\alpha)}$ and detector coupling coefficients $\ln A^{(\beta)}$, $\varphi^{(\beta)}$ to each of the source and detector sites. The values of the coupling coefficients are drawn from Gaussian-distributed random samples. We consider three cases of increasing severety of coupling noise. In addition to the coupling effects, random Gaussian noise with a standard deviation of 1.0% of the data values, simulating measurement shot noise, was added to the data. As a best-case scenario, reconstructions from data including coupling noise, but excluding the random noise, are also presented for comparison. The noise parameters of the resulting six data sets are listed in Table 1.

Figure 3 shows an example of the boundary projection data obtained from one source after the coupling coefficients have been applied for each of the three cases.

The synthetic data are then applied to the Gauss–Newton reconstruction scheme defined in Eq. (12). To assess the effect of the coupling coefficient reconstruction, we perform reconstructions both excluding and including the recovery of the coupling coefficients, with and without additional random noise. In all cases the reconstructions start from an initial estimate of the optical parameters of $\mu_a = 0.025\ \mathrm{mm}^{-1}$ and $\mu_s = 2\ \mathrm{mm}^{-1}$. In the case of coupling coefficient reconstruction the initial estimate of all coupling coefficients $\ln A^{(\alpha,\beta)}$ and $\varphi^{(\alpha,\beta)}$ is 0. For the regularization functional ψ we choose a first-order Tikhonov scheme. Hyperparameter τ is set to 10^{-5} for coupling cases 1 and 2 and to 10^{-4} for case 3.

When applying the data contaminated with coupling coefficients to a conventional reconstruction scheme that recovers the distribution of optical coefficients only, by employing the forward model f, the coupling errors will manifest themselves as artifacts in the recovered μ_a and μ_s images. Inclusion of the coupling coefficients in the reconstruction process, using the extended model $\tilde{f}$ instead, is expected to reduce or eliminate the amount of image artifact.

Figure 4 shows reconstruction results for the three cases of coupling contamination of the measurement

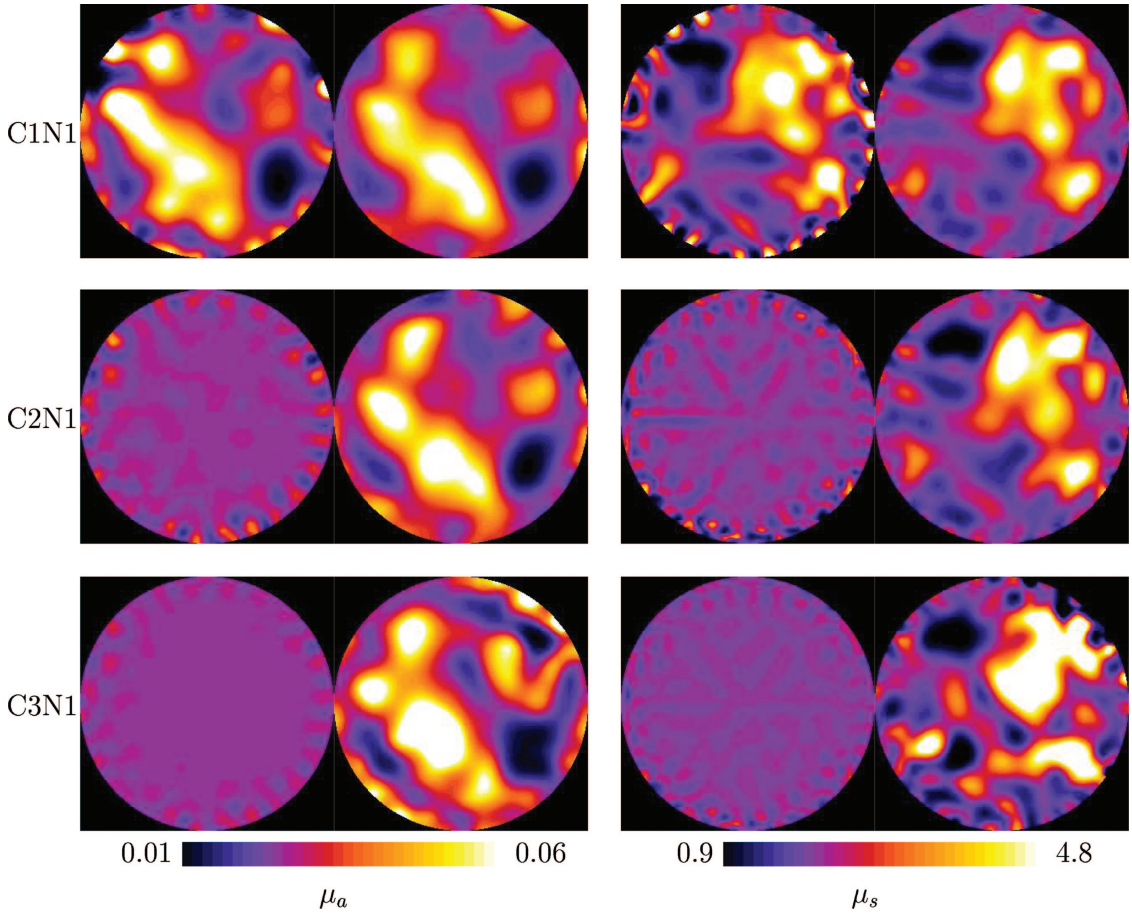

Fig. 5. (Color online) Reconstructions from data in the presence of coupling and random errors. The arrangement of images is the same as for Fig. 4.

data, when reconstructed both with and without recovering the coupling coefficients. It can be seen that the presence of coupling coefficients severely degrades the image quality of the conventional reconstructions with loss of localization of the inclusions and the appearance of boundary artifacts. When the coupling coefficients are reconstructed together with the optical parameters, the results are significantly improved. For cases 1 and 2 the image quality is comparable with that achieved from uncontaminated data. In case 3 the images begin to deteriorate but still provide significant improvement in localization compared to a reconstruction that ignores the coupling coefficients.

When additional random noise is added to the data sets, the resulting reconstructions of both the images and coupling coefficients are affected. The images are therefore degraded not only by the statistical noise but also by the cross talk from the incompletely recovered coupling coefficients. Therefore we expect the effect of the coupling reconstruction to decrease at higher levels of random noise. Figure 5 shows reconstructions from data degraded by coupling and random noise. The inclusion of the coupling coefficients in the reconstructions still significantly improves the quality of the recovered images, even though the contrast and edge localization of the inclusions is reduced compared with the case without random noise. The amount of boundary artifact is also increased, indicating that residual coupling errors are affecting the images.

The reconstructed coupling coefficients are shown in Fig. 6. The results for case 1 are scaled by a factor of 10 and those for case 2 by a factor of 2 so that they can be compared with the same target coefficients. It can be seen that the coefficients are recovered very well in all cases.

The L_2 errors of the recovered coupling coefficients with respect to the target values are shown in Fig. 7 as functions of iteration count. For moderate coupling targets (case C1N0), the coefficients are well recovered after approximately ten iterations, while convergence is slower for case C2N0. For the most severe coupling coefficients (case C3N0) the residual error of the recovered coupling coefficients remains significantly higher. The addition of Gaussian random noise on the data results in an increase of the residual error of the recovered coupling coefficients in all three cases (bottom graph of Fig. 7).

Figure 8 shows the convergence of the reconstruction cost functions for all three cases as a function of iteration count for the data without additional random noise (top graph) and with random noise on the data (bottom graph). We find again that cases C1 and

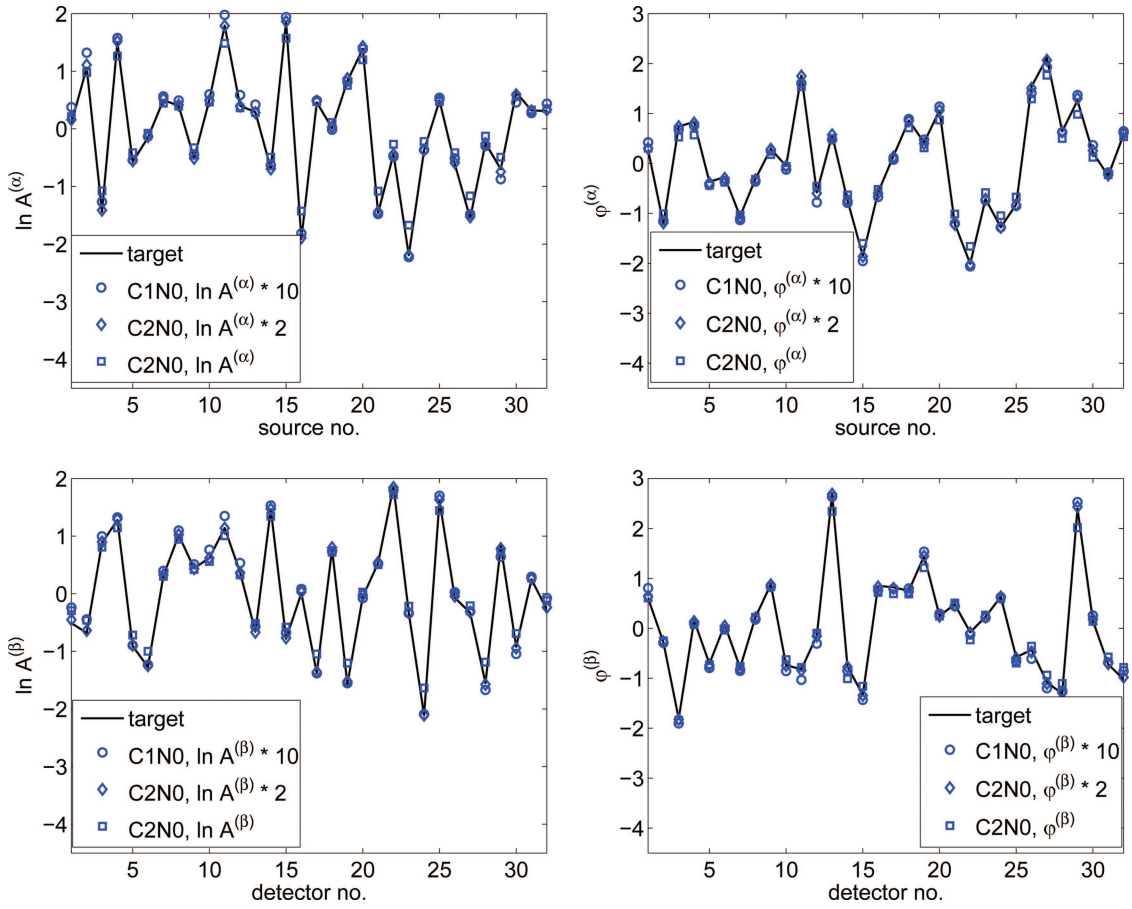

Fig. 6. (Color online) Reconstructed source and detector coupling coefficients for $\ln A$ and φ. The results for cases 1, 2, and 3 are scaled so that they can be compared to common target coefficients (solid curve).

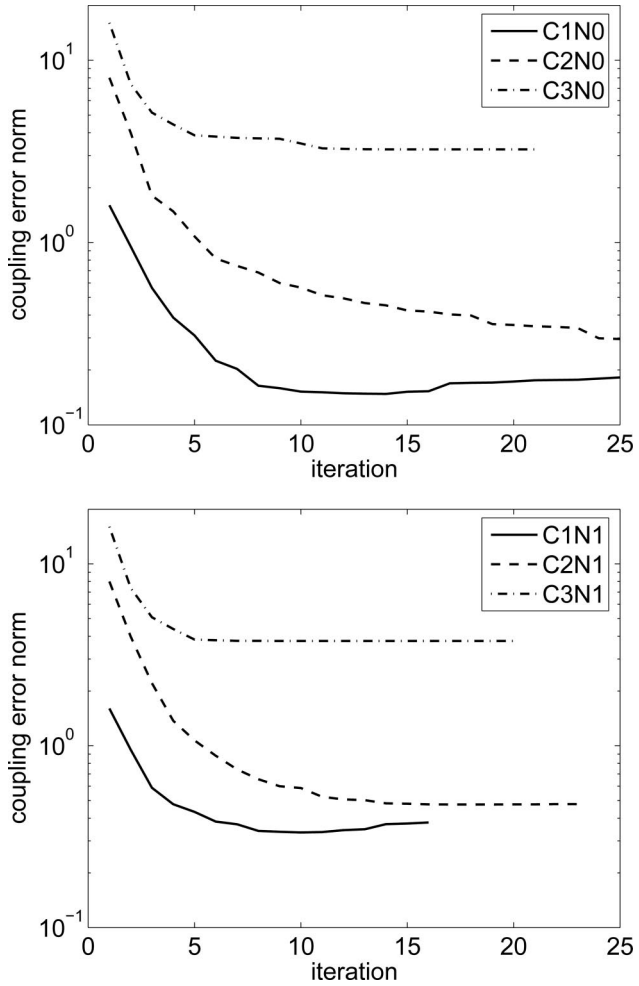

Fig. 7. L_2 error of reconstructed coupling coefficients as a function of iteration count for the three cases considered. Top, results from data without additional random noise. Bottom, results from data with additional 0.5% Gaussian-distributed random noise.

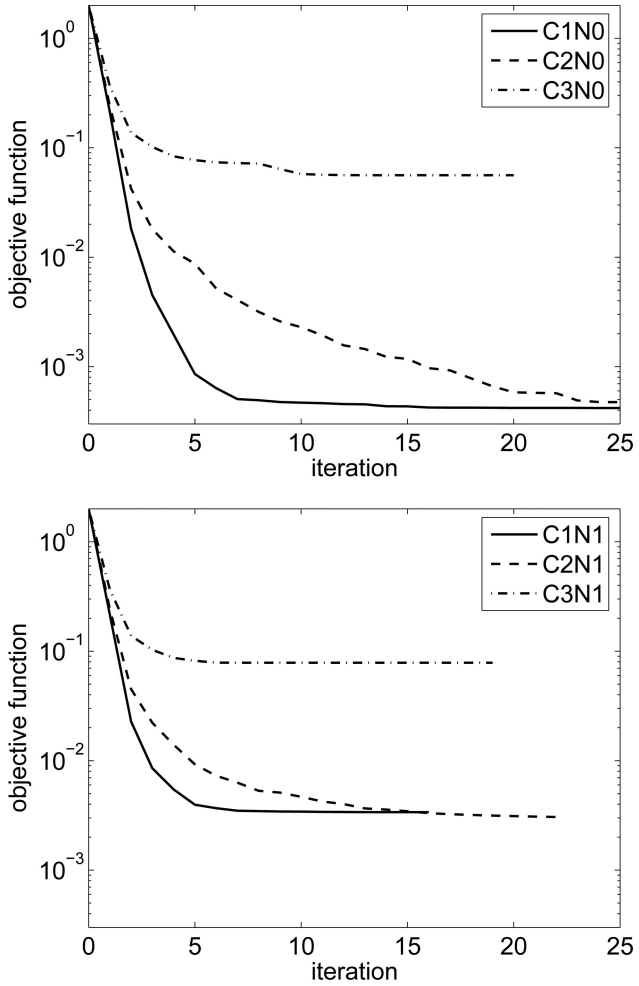

Fig. 8. Objective functions for the three coupling cases as a function of iteration count. Top, no additional random data noise (N0). Bottom, 0.5% Gaussian-distributed random data noise.

C2 converge to similar residuals, although at different rates, while in case C3 the residual remains significantly higher. Similarly, the residuals for the noisy data are higher than for the noiseless data in all three cases.

To assess the effect of the coupling reconstruction on superficial perturbations, a further simulation was performed on a homogeneous circular mesh with a single semicircular absorption perturbation of radius 3 mm located directly under a source site [Fig. 9(a)]. Data without coupling or random noise contamination for 32 source and 32 detector sites were then generated and used for reconstructions both excluding and including coupling coefficients. Cross sections through the target absorption image and both reconstructed absorption images are shown in Fig. 9(b). The reconstructed amplitude and phase coupling coefficients are shown in Fig. 10. As can be seen in the case of reconstructing for the coupling coefficients, the surface perturbation is partly assimilated into the coupling coefficients, leading to an underestimation of the reconstructed object contrast and spurious coupling coefficients on the sources and detectors close to the object. Sometimes this effect of suppressing superficial features in the reconstructed images will be desirable to suppress boundary artifacts, e.g., from local variation in skin pigmentation. However, in situations where superficial objects must be detected, for example, in optical mammography, where it is frequently the case that the tumor is located near the surface, this method is not applicable.

B. Experimental Phantom Data

To test the effectiveness of the coupling parameter reconstruction with realistic data, reconstructions were performed with data obtained with an experimental frequency domain instrument[19] from a cylindrical phantom with embedded inclusions. The effect of coupling errors was simulated by placing hair between the phantom surface and the tips of the fiber optics delivering light from the sources and collecting light at the detectors. Hair is one of the most likely sources of coupling variations when optodes are placed on the head for data acquisition in brain imaging.

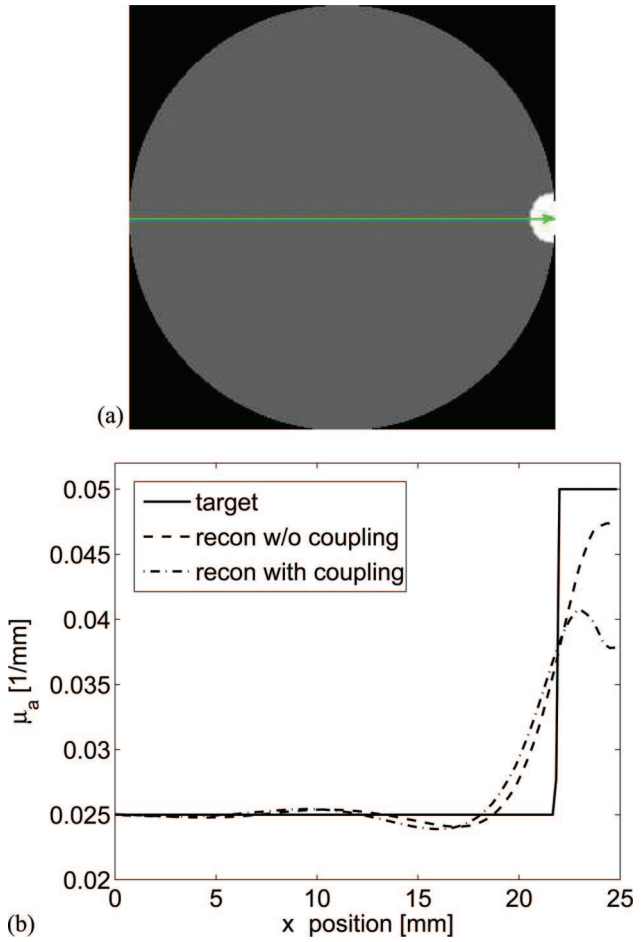

Fig. 9. (Color online) Effect of coupling coefficient reconstruction on the recovery of a superficial perturbation. (a) Target image with boundary absorption inclusion. (b) Cross sections of the target and reconstructed absorption images along the line indicated in (a).

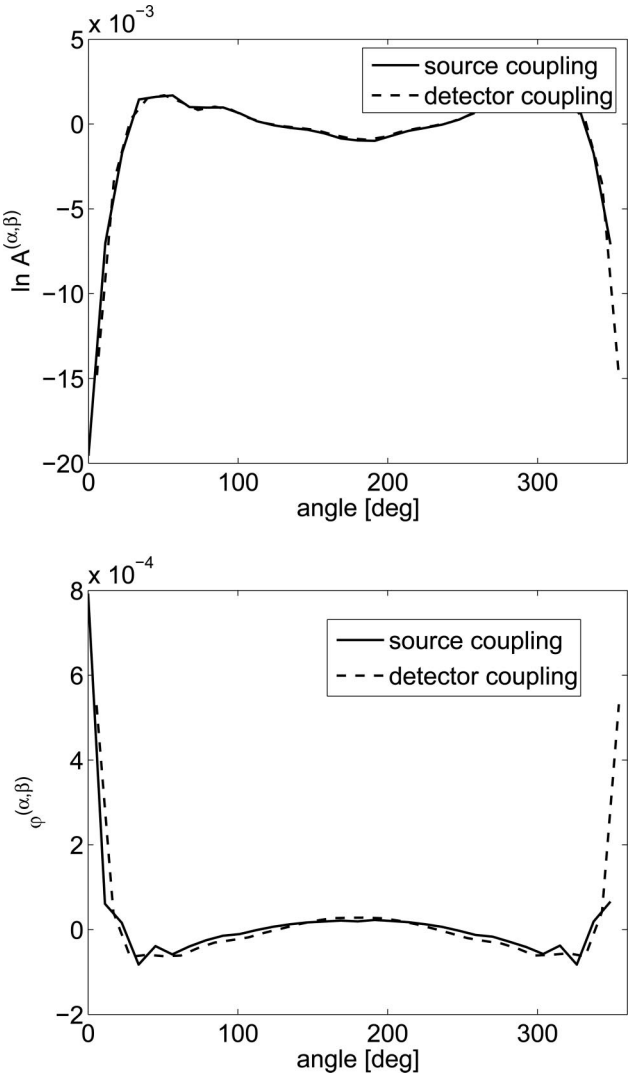

Fig. 10. (Color online) Reconstructed coupling coefficients of log amplitude (top) and phase (bottom) for the superficial inclusion in Fig. 9.

The phantom had a diameter of 70 mm and a height of 110 mm. It consisted of a homogeneous background material with $\mu_a \approx 0.01\ \mathrm{mm}^{-1}$ and $\mu_s' \approx 1\ \mathrm{mm}^{-1}$. One of the two small cylindrical inclusions had a contrast of $\times 2$ in μ_a, the other a contrast of $\times 2$ in μ_s'. A second, homogeneous cylinder with identical background parameters was used to obtain baseline measurement used for difference image reconstructions.

Sixteen source and sixteen detector fibers were arranged with equal angular spacing in two rings around the cylinder mantle above and below the central plane, as shown in Fig. 11. Only 15 of the detectors were used because of a technical problem with one of the detector channels. For each source the measurements from the four closest detectors were discarded to reduce boundary artifacts that can arise as a result of mismatches between model and measurement data projected into spacially localized sensitivity regions. This leads to a total of 180 measurements, where each measurement consisted of the amplitude and phase of the transilluminated signal, arising from source input amplitude modulated at 100 MHz.

Figure 12 shows a subset of the difference data vectors between inhomogeneous and homogeneous phantoms for both log amplitude (top graph) and phase measurements (bottom graph). It compares the coupling-free case (no hair under the optodes) with the coupling case (hair was placed between all fiber tips and the phantom surface). It can be seen that the effect of coupling errors is higher in log amplitude than in phase. For the log amplitude data the effect of the coupling errors is significantly higher than the effect of the inclusion. For the phase data the coupling effect is comparable in magnitude to the perturbations caused by the inclusions, except for some spikes on the coupling data for a few measurements.

To construct a forward model, the cylinder was discretized by a finite-element mesh consisting of 181,278 tetrahedral elements and 35,228 nodes, with the node density highest at the surface of the mesh.

The initial parameter distributions for the reconstructions were set to homogeneous values of

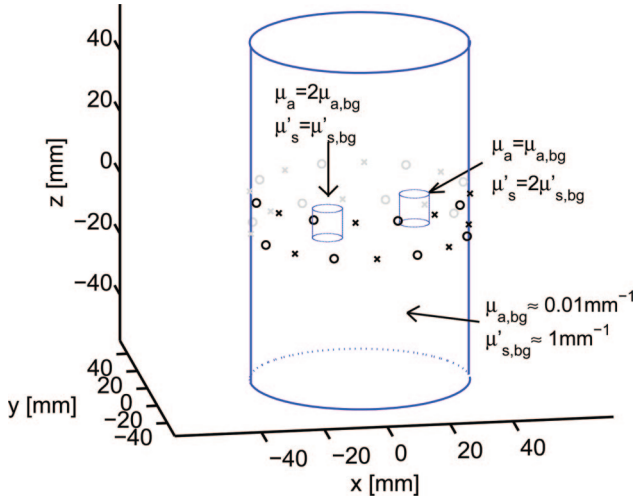

Fig. 11. (Color online) Phantom setup for experimental data acquisition: location of embedded inclusions and arrangement of sources and detectors on the surface.

$\mu_a = 0.0103\ \text{mm}^{-1}$ and $\mu_s' = 0.807\ \text{mm}^{-1}$. These initial values were obtained by a global homogeneous parameter reconstruction from the measurements.

1. *Difference Reconstructions*

We first consider the case of difference imaging, where two sets of data, representing two different states of the probed medium, are acquired, and the reconstruction recovers the parameter differences. In this phantom experiment, a baseline measurement was performed on a homogeneous cylinder that did not contain the inclusions. The baseline measurement was acquired without coupling contamination, while the measurements of the inhomogeneous cylinder were obtained both with and without hair under the optodes.

Reconstruction in dynamic imaging is performed by calculating projection data $f(\mathbf{x}_0)$ for the initial parameter estimate $\mathbf{x}_0$ and adding the measured difference data $\mathbf{y}^{(\text{inhomog})} - \mathbf{y}^{(\text{homog})}$ to obtain a synthetic absolute measurement $\mathbf{y} = f(\mathbf{x}_0) + \mathbf{y}^{(\text{inhomog})} - \mathbf{y}^{(\text{homog})}$. Note that in situations where $\mathbf{y}^{(\text{inhomog})}$ and $\mathbf{y}^{(\text{homog})}$ are contaminated with the same coupling coefficients, these effects cancel in the difference data, and the reconstruction of the coupling coefficients is less critical.

Figure 13 shows cross sections of dynamic reconstructions of absorption (top row) and scattering distribution (bottom row) in the central plane of the cylinder. The left column is a reconstruction from the inhomogeneous cylinder acquired without hair. The middle column shows reconstructions from data with hair but without recovery of the coupling coefficients. The right column used the same data for the reconstruction but also recovered the coupling coefficients. We find that the effect of coupling contamination of the data leads to a reduction of contrast (in the scattering image) and localization (in the absorption image) if the coupling coefficients are not reconstructed. The inclusion of the coupling coefficients in the reconstruction recovers contrast and localization well although some residual boundary artifacts in absorption and scattering remain.

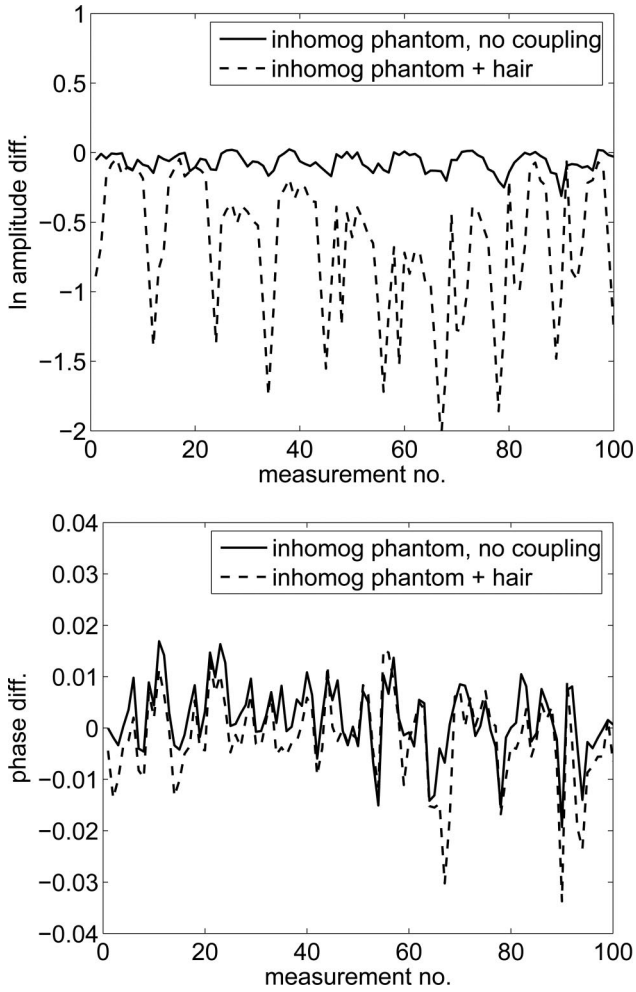

Fig. 12. Subset of 100 measurements of the experimental data vectors of log amplitude (top) and phase (bottom). Shown are the data differences between inhomogeneous and homogeneous phantom for the two cases with and without hair under the optodes.

2. *Absolute Reconstructions*

Absolute reconstructions from measurement data are required where no baseline data are available and if absolute values of absorption and scattering must be recovered. The same data from the inhomogeneous cylinder as in the previous section are used, both with and without coupling contamination with hair.

Cross sections of the reconstructed absolute parameter distributions are shown in Fig. 14 for absorption (top row) and scattering coefficients (bottom row). Because of the large differences in dynamic range between the reconstructions, the images were scaled individually. The images in the left column show the reconstruction from data without coupling contamination. Both inclusions are recovered although at lower contrast and with more artifacts in the background medium than for the corresponding difference recon-

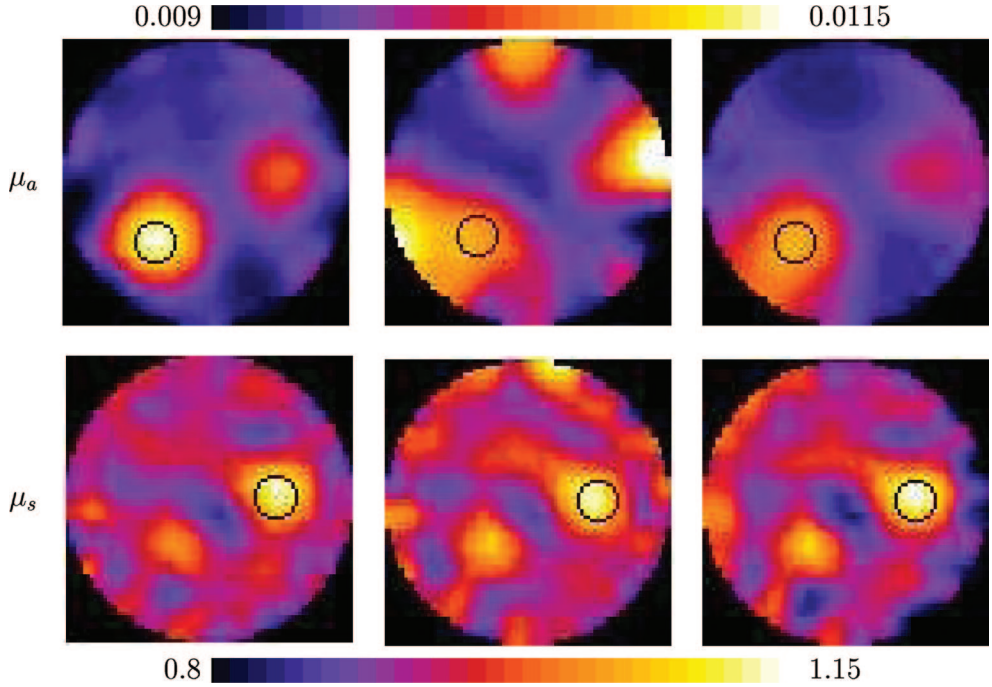

Fig. 13. (Color online) Cross sections of reconstruction of absorption (top) and scattering distributions (bottom) from difference phantom data. Columns from left to right, reconstruction of uncontaminated data, reconstruction of hair data without recovery of coupling coefficients, reconstruction of hair data with coupling coefficients. Target locations are marked with a black circle.

struction. In particular, the scattering image suffers from boundary artifacts similar in magnitude to the recovered target object. The central column of images shows the reconstruction results from data with coupling coefficients induced by hair under the optodes, where the coupling coefficients were not reconstructed. In this case the reconstruction fails entirely with complete loss of the inclusions, and the appearance of high-contrast boundary artifacts under individual optode positions. When the coupling coefficients

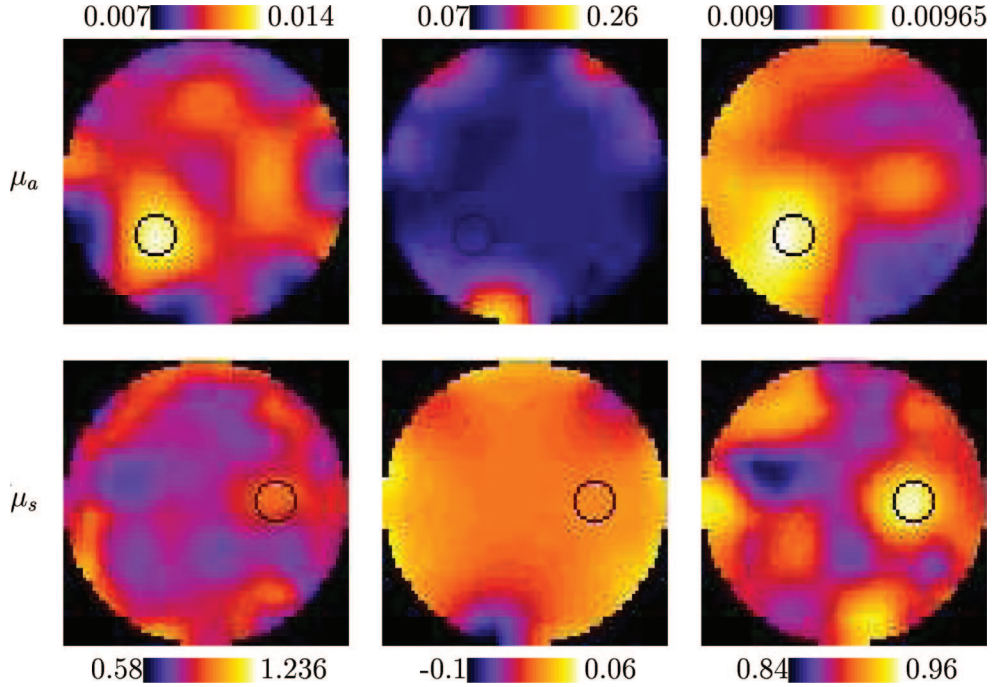

Fig. 14. (Color online) Cross sections of reconstructions of absorption (top) and scattering distributions (bottom) from absolute phantom data. Columns from left to right, reconstruction of uncontaminated data, reconstruction of hair data without recovery of coupling coefficients, reconstruction of hair data with coupling coefficients. Target locations are marked with a black circle.

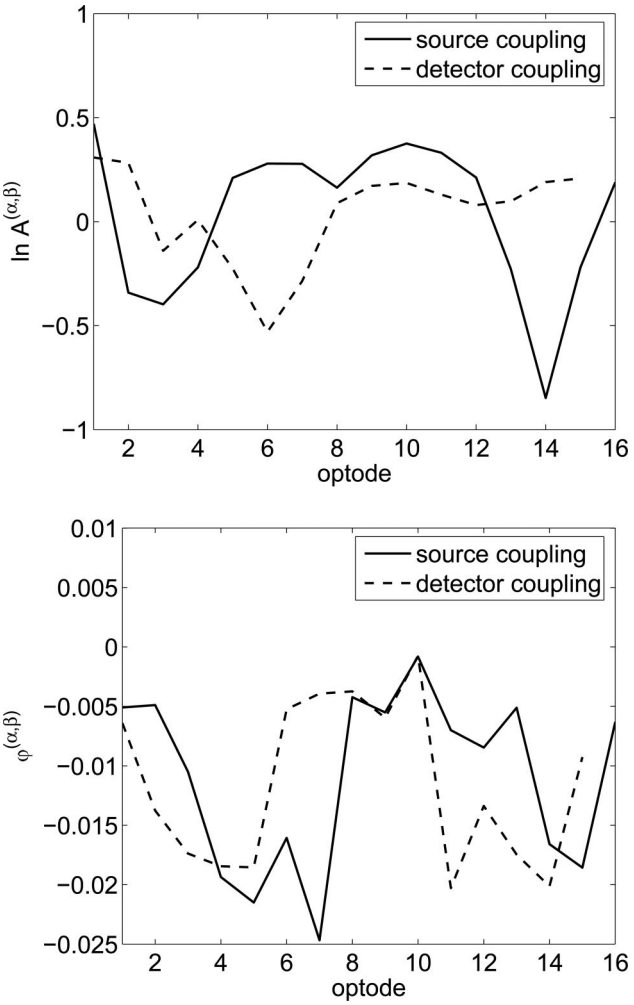

Fig. 15. Source and detector coupling coefficients ln $A^{(\alpha,\beta)}$ (top) and $\varphi^{(\alpha,\beta)}$ (bottom) recovered during absolute reconstruction of experimental phantom data.

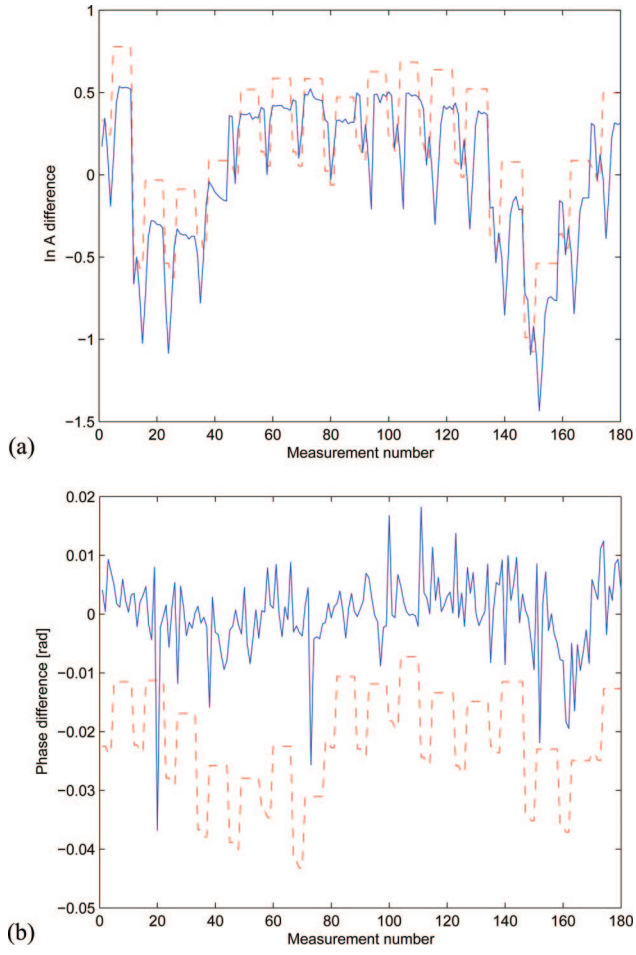

Fig. 16. (Color online) Effect of hair on the difference data for (a) log A, (b) phase. Dashed curve is the product of source and detector coupling coefficients obtained in the reconstruction; solid curve is the measured difference between clean measurement of the inhomogeneous phantom and a measurement where the hair is in place.

are reconstructed (right column), both inclusions can be recovered well again, although at some loss of contrast. The absorption object exhibits slight bleeding toward the boundary, similar to the difference reconstruction case. Interestingly, the recovery of the scattering inclusion appears improved compared with the reconstruction from uncontaminated data. This may be attributable to the presence of coupling effects in the experimental system other than the deliberate effects caused by inserting hair.

The recovered coupling coefficients are shown in Fig. 15. It can be seen that the predicted magnitude of the coupling coefficients is significantly larger than the influence of the inclusions on the boundary data (cf. Fig. 12), which explains the large effect of the coupling reconstructions on the recovered images. To provide an estimate of the quality of the recovered coupling coefficients, we compare in Fig. 16 the product of the reconstructed source and detector coupling coefficients with the effect of the hair on the measured data. The spatial variability of the amplitude coefficients is reconstructed well. The corresponding graph for phase coefficients shows a less perfect match. This is because of greater noise in the phase measurement and the lack of an explicit cause of large phase coupling effects in the data. The reconstruction of the phase coupling coefficients in this experiment also corrected some residual calibration errors owing to the low optical power of the calibration measurements.

5. Conclusions

We have presented a method to address the problem of reconstruction artifacts in optical tomography arising from the effects of coupling losses in the complex-valued measurement data collected by data acquisition systems. In this context, the term coupling loss combines all types of measurement error that are specific to individual source and detector sites. This type of measurement error is well known to be a problem in optical tomography, in particular where fiber optics are used for light delivery and where hair under the optode tips, moisture, or air gaps can lead to atten-

uation of the detected signal. Other sources of coupling errors not specific to fiber-optic acquisition systems include differences in power or sensitivity of individual light sources and detectors. Coupling errors are difficult to quantify and therefore cannot generally be incorporated into the forward model. Instead, the coupling coefficients are treated as unknowns and appended to the solution space.

The method presented here considers coupling errors in both amplitude and phase data, which are reconstructed simultaneously with the volume distributions of absorption and diffusion coefficients.

We have shown reconstructions from simulated 2D data, which were contaminated with synthetic coupling errors, and demonstrated that the reconstructions can be improved significantly even in severe cases where the level of coupling errors causes a conventional reconstruction to fail entirely.

The algorithm was then applied to experimental phantom data where coupling errors were simulated by placing hair between the phantom surface and the fiber tips of source and detector fiber optics. We have performed reconstructions from both difference data and absolute reconstructions and demonstrated that in both cases the inclusion of the coupling coefficients in the reconstruction can lead to improvements that reduce artifacts and restore the ability to recover the inhomogeneities in optical coefficients.

The authors acknowledge grant support from the Engineering and Physical Sciences Research Council, grants GR/N148/01 and GR/S48837/02, and from the Medical Research Council.

References

1. D. Grosenick, H. Wabnitz, and H. Rinneberg, "Time-resolved imaging of solid phantoms for optical mammography," Appl. Opt. **36,** 221–231 (1997).
2. A. Yodh and B. Chance, "Spectroscopy and imaging with diffusing light," Phys. Today **48**(3), 34–40 (1995).
3. A. P. Gibson, J. Hebden, and S. R. Arridge, "Recent advances in diffuse optical tomography," Phys. Med. Biol. **50,** R1–R43 (2005).
4. M. Cope and D. T. Delpy, "System for long term measurement of cerebral blood and tissue oxygenation on newborn infants by near-infrared transillumination," Med. Biol. Eng. Comput. **26,** 289–294 (1988).
5. D. Hawysz and E. M. Sevick-Muraca, "Developments towards diagnostic breast cancer imaging using near–infrared optical measurements and fluorescent contrast agents," Neoplasia **2,** 388–417 (2000).
6. D. A. Boas, D. H. Brooks, E. L. Miller, C. A. DiMarzio, M. Kilmer, R. J. Gaudette, and Q. Zhang, "Imaging the body with diffuse optical tomography," IEEE Signal Process Mag. **18**(6), 57–75 (2001).
7. B. W. Pogue, K. D. Paulsen, C. Abele, and H. Kaufman, "Calibration of near-infrared frequency-domain tissue spectroscopy for absolute absorption coefficient quantitation in neonatal head-simulating phantoms," J. Biomed. Opt. **5,** 185–193 (2000).
8. Y. Bluestone, G. Abdoulaev, C. H. Schmitz, R. L. Barbour, and A. H. Hielscher, "Three-dimensional optical tomography of hemodynamics in the human head," Opt. Express **9,** 272–286 (2001).
9. A. P. Gibson, T. Austin, N. L. Everdell, M. Schweiger, S. R. Arridge, J. H. Meek, J. S. Wyatt, D. T. Delpy, and J. C. Hebden, "Three-dimensional whole-head optical tomography of passive motor evoked responses in the neonate," Neuroimage **30,** 521–528 (2005).
10. M. Schweiger, S. R. Arridge, and I. Nissilä, "Gauss–Newton method for image reconstruction in diffuse optical tomography," Phys. Med. Biol. **50,** 2365–2386 (2005).
11. D. A. Boas, T. J. Gaudette, and S. R. Arridge, "Simultaneous imaging and optode calibration with diffusive optical tomography," Opt. Express **8,** 263–270 (2001).
12. J. J. Stott, J. P. Culver, S. R. Arridge, and D. A. Boas, "Optode positional calibration in diffuse optical tomography," Appl. Opt. **42,** 3154–3162 (2003).
13. C. H. Schmitz, H. L. Graber, H. Luo, I. Arif, J. Hira, Y. Pei, A. Bluestone, S. Zhong, R. Andronica, I. Soller, N. Ramirez, S.-L. S. Barbour, and R. L. Barbour, "Instrumentation and calibration protocol for imaging dynamic features in dense-scattering media by optical tomography," Appl. Opt. **39,** 6466–6486 (2000).
14. S. Oh, A. B. Milstein, R. P. Millane, C. A. Bouman, and K. J. Webb, "Source-detector calibration in three-dimensional Bayesian optical diffusion tomography," J. Opt. Soc. Am. A **19,** 1983–1993 (2002).
15. A. Gibson, R. M. Yusof, H. Deghani, J. Riley, N. Everdell, R. Richards, J. C. Hebden, M. Schweiger, S. R. Arridge, and D. T. Delpy, "Optical tomography of a realistic neonatal head phantom," Appl. Opt. **42,** 3109–3116 (2003).
16. T. O. McBride, B. W. Pogue, U. L. Österberg, and K. D. Paulsen, "Strategies for absolute calibration of near-infrared tomographic tissue imaging," in *Oxygen Transport to Tissue XXIV,* J. F. Dunn and H. M. Swartz, eds. (Kluwer/Plenum, 2003), pp. 85–99.
17. C. Li and H. Jiang, "A calibration method in diffuse optical tomography," J. Opt. A **6,** 844–852 (2004).
18. T. Tarvainen, V. Kolehmainen, M. Vauhkonen, A. Vanne, A. P. Gibson, M. Schweiger, S. R. Arridge, and J. P. Kaipio, "Computational calibration method for optical tomography," Appl. Opt. **44,** 1879–1888 (2005).
19. I. Nissilä, T. Noponen, K. Kotilahti, T. Tarvainen, M. Schweiger, L. Lipiäinen, S. R. Arridge, and T. Katila, "Instrumentation and calibration methods for the multichannel measurement of phase and amplitude in optical tomography," Rev. Sci. Instrum. **76,** 044302 (2005).
20. A. Ishimaru, *Wave Propagation and Scattering in Random Media* (Academic, 1978), Vol. 1.
21. R. C. Haskell, L. O. Svaasand, T.-T. Tsay, T.-C. Feng, M. S. McAdams, and B. J. Tromberg, "Boundary conditions for the diffusion equation in radiative transfer," J. Opt. Soc. Am. A **11,** 2727–2741 (1994).
22. S. R. Arridge, "Optical tomography in medical imaging," Inverse Probl. **15,** R41–R93 (1999).
23. M. S. Patterson, B. Chance, and B. C. Wilson, "Time resolved reflectance and transmittance for the noninvasive measurement of tissue optical properties," Appl. Opt. **28,** 2331–2336 (1989).
24. O. Dorn, "A transport-backtransport method for optical tomography," Inverse Probl. **14,** 1107–1130 (1998).
25. A. D. Klose and A. H. Hielscher, "Iterative reconstruction scheme for optical tomography based on the equation of radiative transfer," Med. Phys. **26,** 1698–1707 (1999).
26. S. R. Arridge, M. Schweiger, M. Hiraoka, and D. T. Delpy, "A finite element approach for modeling photon transport in tissue," Med. Phys. **20,** 299–309 (1993).
27. M. Schweiger, S. R. Arridge, M. Hiraoka, and D. T. Delpy, "The finite element model for the propagation of light in scattering media: boundary and source conditions," Med. Phys. **22,** 1779–1792 (1995).